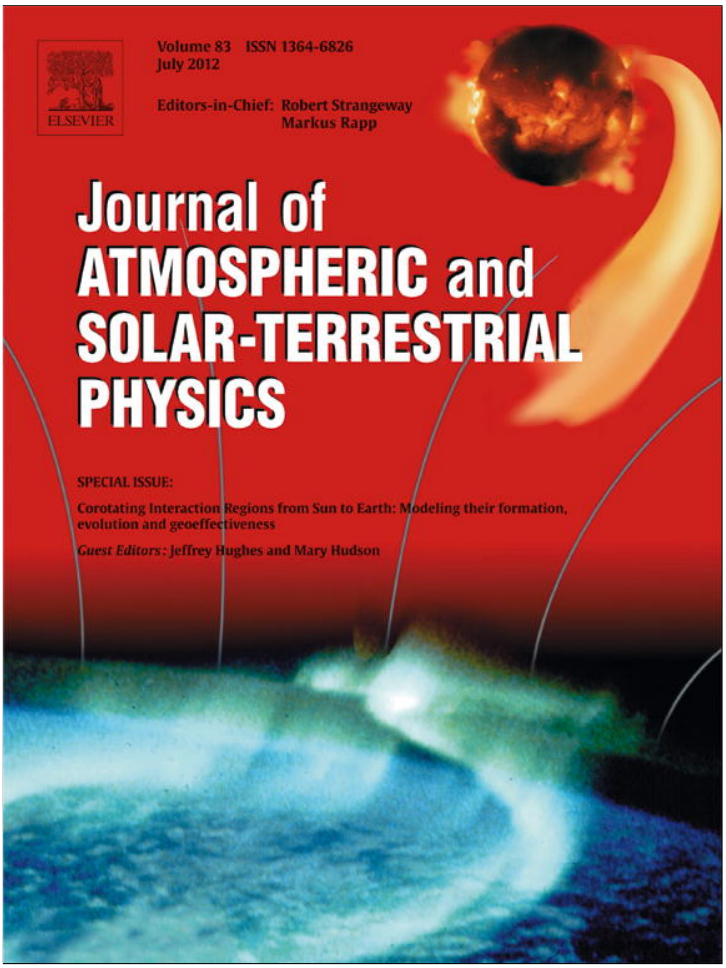

Journal of Atmospheric and Solar-Terrestrial Physics 83 (2012) 1–10

Contents lists available at SciVerse ScienceDirect

Journal of Atmospheric and Solar-Terrestrial Physics

journal homepage: www.elsevier.com/locate/jastp

Corotating interaction regions during the recent solar minimum: The power and limitations of global MHD modeling

Pete Riley *, Jon A. Linker, R. Lionello, Z. Mikic

Predictive Science, Inc., 9990 Mesa Rim Road, San Diego, CA, United States

ARTICLE INFO

Article history:
Received 4 September 2011
Received in revised form
12 November 2011
Accepted 15 December 2011
Available online 14 January 2012

Keywords:
Corona
Solar wind
Corotating interaction regions
Magnetohydrodynamics
Space weather

ABSTRACT

The declining phase of solar activity cycle 23 has provided an unprecedented opportunity to study the evolution and properties of corotating interaction regions (CIRs) during unique and relatively steady conditions. The absence of significant transient activity has allowed modelers to test ambient solar wind models, but has also challenged them to reproduce structure that was qualitatively different than had been observed previously (at least within the space era). In this study, we present and analyze global magnetohydrodynamic (MHD) solutions of the inner heliosphere (from $1R_S$ to 1 AU) for several intervals defined as part of a Center for Integrated Space weather Modeling (CISM) interdisciplinary campaign study, and, in particular, Carrington rotation 2060. We compare *in situ* measurements from ACE and STEREO A and B with the model results to illustrate both the capabilities and limitations of current numerical techniques. We show that, overall, the models do capture the essential structural features of the solar wind for specific time periods; however, there are times when the models and observations diverge. We describe, and, to some extent assess the sources of error in the modeling chain from the input photospheric magnetograms to the numerical schemes used to propagate structure through the heliosphere, and speculate on how they may be resolved, or at least mitigated in the future.

1. Introduction

Corotating interaction regions (CIRs) and coronal mass ejections (CMEs) are the dominant forces that shape the large-scale structure of the heliosphere. While CMEs are intrinsically transient phenomena, CIRs are assumed to be quasi-stationary. In fact, strictly speaking, CIRs are structures that remain stationary forever in a frame corotating with the Sun. In reality, of course, the processes that produce the slow and fast solar wind are always in flux and the concept of CIRs is an idealization. When dynamically interacting structures appear in the solar wind but do not obviously reappear from one rotation to the next, they may be more strictly labeled stream interaction regions (e.g., Lindsay et al., 1995).

The study of CIRs is important for a number of reasons. First, beyond their intrinsic scientific value, CIRs generate shocks capable of accelerating energetic particles (e.g., Lario and Roelof, 2007). Second, at Earth, they are associated with recurrent geomagnetic activity (e.g. Tsurutani et al., 2006) and may enhance the strength of non-recurrent storms (e.g., Gosling et al., 1990). Third, because, over the last 40 years or so, we have developed a good basic understanding of them, we believe that CIR phenomena may be accessible to physics-based prediction within the foreseeable future (e.g., Riley et al., 2001b).

CIRs form because the plasma expelled from the Sun has a range of speeds. A slow parcel of plasma is compressed by faster plasma behind, creating a region of compression, while faster plasma outrunning slower plasma behind creates an expansion wave, or rarefaction region. Given simple velocity profiles close to the Sun, it is straightforward to infer the basic large-scale properties (at least in a qualitative sense) farther out in the solar wind (Riley et al., this issue). Global heliospheric MHD models can be driven by realistic velocity profiles, computed from coronal MHD solutions, producing a rich and often complex pattern of compression and rarefaction regions (Riley et al., 2011). Often, but not always, the modeled solutions match *in situ* measurements (Riley et al., 2001a).

The declining phase of solar cycle 23, culminating in the prolonged solar minimum that occurred in late 2008, has provided an unprecedented opportunity to study CIR structure in the solar wind in the relative absence of CMEs and other obvious transient phenomena (Riley et al., 2011). As such, it has allowed modelers to test their basic input parameters and model assumptions under pristine conditions (Gibson et al., 2009, 2011). However, this period also produced a number of features that, at least within the span of the space era, were also unique.

* Corresponding author. Tel.: +1 8582175868; fax: +1 8584501953.
E-mail address: pete@predsci.com (P. Riley).

1364-6826/$ - see front matter © 2011 Elsevier Ltd. All rights reserved.
doi:10.1016/j.jastp.2011.12.013

Thus the models have also been challenged to operate in what may be a new environment, raising questions about whether the assumptions made and parameters determined from previous minima hold under these new conditions.

The Center for Integrated Space Weather Modeling (CISM) defined a campaign study to understand the properties of CIRs in the corona and inner heliosphere and their effects throughout the magnetosphere and all the way down to the atmosphere. One of the time periods selected was Carrington rotation (CR) 2060, which occurred between August 14 and September 10, 2007. In this study, we use a global MHD model of the inner heliosphere to define and interpret CIR structure (out to 1 AU) during this interval, as well as other portions of the declining phase of solar cycle 23. In a complementary paper, Wiltberger et al. (this issue) describes a study in which a global magnetospheric model was driven directly with output from the model results that are the subject of the present paper. Stevens et al. (this issue) also provide a complementary analysis of the MHD solutions during the recent solar minimum as well as the previous one, focusing on resolving a long-standing issue with respect to the low interplanetary magnetic field values predicted by global models. In two related studies, we also describe the structure of the heliosphere, including the formation and evolution of CIRs during the "Whole Heliosphere Interval," which occurred between March 19 and April 16, 2007 (Riley et al., 2010a, 2011) as well as more generally during the recent minimum (Riley, 2010). Finally, in this volume, Riley et al. (this issue) use global MHD model results to interpret some properties of stream interfaces (SIs) and CIR-associated shocks observed over solar cycle 23, and particularly during the recent minimum.

In the sections below, we summarize our numerical approach for modeling the large-scale structure of the quasi-stationary inner heliosphere and then present a selection of results to illustrate some of the distinguishing features of the declining phase of solar cycle 23 and the ensuing minimum. We then compare the model results directly with *in situ* measurements by the ACE and STEREO A/B spacecraft and use the model results to provide a global picture of these localized observations. Our comparisons demonstrate that this type of modeling approach can be successful in reproducing the large-scale features suggested by the observations, but also highlights a number of caveats and limitations that must be borne in mind when interpreting the solutions. We discuss each of these in detail and suggest how future developments may address them and lead to better models of the ambient solar wind, ultimately, with predictive capabilities.

2. Modeling approach

Over the last two decades, our group has developed, refined, and applied a number of numerical models for studying the Sun's corona and the heliosphere. As with any model, to make meaningful inferences from the solutions, it is crucial to understand: the assumptions that go into the model; how the boundary conditions are produced; and, in some cases, the numerical schemes that are implemented to solve what are hopefully the relevant equations. To contrast two approaches, we continue to employ both polytropic (Riley et al., 2001a) and thermodynamic (Lionello et al., 2009) coronal models, which treat the energy transport processes in the corona in radically different ways. They trade simplicity and computational requirements for potentially vital physics. However, it is not always the case that the more sophisticated algorithm produces better results. In the case of the polytropic solutions, for example, the fact that they produce remarkably good solutions for the structure of the coronal magnetic field, at the expense of poorer velocity profiles, has led us to develop an *ad hoc* technique for deriving the boundary conditions for the heliospheric model, based on the topology of the magnetic field (Riley et al., 2001a). While we anticipate that a heliospheric model driven directly by output from a thermodynamic solution will ultimately produce more accurate interplanetary solutions, at present, the *ad hoc* prescription typically performs better (of course, the *ad hoc* technique can be used with thermodynamic solutions as well as polytropic solutions; however, this results in a significant computational cost for an arguably marginal gain in the quality of the coronal magnetic field solution).

In this study, we use the CORHEL (CORona-HELiosphere) package; a coupled suite of solar and heliospheric MHD and PFSS models developed by scientists at PSI, Boston University, NOAA, NASA/GFSC, Dartmouth College, and APL. CORHEL aims to supply a simple, coherent interface to these models and includes simple coupling routines so that the output of one model can be used to drive another. Fig. 1 summarizes the main components of CORHEL as well as highlighting areas for potential future development. The chain begins by choosing a photospheric magnetic field map, formatted as a synoptic (or, strictly speaking a diachronic) map of longitude–latitude values covering an entire solar rotation, from one of several solar observatories. In *step*1, the magnetogram is processed in such a way that it can be used to drive the MHD model. This includes: (1) if necessary, converting the measured line-of-sight field to a radial field, assuming that the observed field is everywhere radial; (2) extrapolating the more-resolved

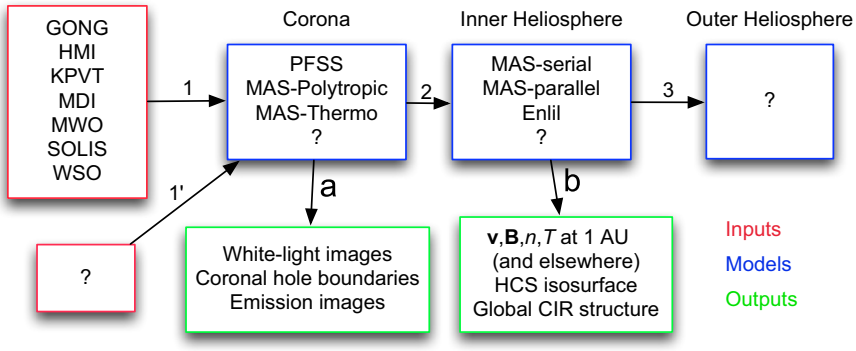

Fig. 1. Flowchart illustrating the inputs, models, and outputs for the CORHEL package. Inputs are shown in red, models in blue, and outputs in green. Potential areas for future development are indicated by the '?' symbols. (For interpretation of the references to color in this figure legend, the reader is referred to the web version of this article.)

mid-latitude fields to the poorly resolved polar regions; and (3) diffusing or filtering the data to a degree that structure relevant to the study is retained but higher frequency features, which might cause numerical issues, are removed. We note that the procedure for processing the magnetograms has undergone significant revision over the last 6 months, and new solutions sometimes depart significantly from previously computed results: typically, but not always, the new results produce a better match with observations. *Step*1 also requires the user to choose appropriate input parameters for the specific coronal model being used. The polytropic version of the coronal model has fewer free parameters than the thermodynamic model, and while this limits the scope of the solutions, we have considerably more experience adjusting them. As noted above, when coupled with the *ad hoc* prescription for deriving the heliospheric model boundary conditions (Riley et al., 2001a), we have found this model usually produces results that are as good as or better than the thermodynamic model, for which much of the underlying physics remains to be explored.

At present, CORHEL supports three coronal models. We have already discussed the MAS polytropic and thermodynamic models. Additionally, we have also implemented a finite-difference potential field source surface (PFSS) model, which includes a current sheet component, and produces speed profiles based on the WSA specification (Arge, personal communication, 2010). Since CORHEL is as much a framework as the models themselves, other coronal models can be easily added provided that they accept (at the least) synoptic maps of the radial component of the photospheric magnetic field, and output (at the least) a global solution for the solar coronal magnetic field.

Step 1′ suggests one of CORHEL's potential opportunities for future growth. Currently, the only observations used to drive the model are line-of-sight measurements of the magnetic field in the photosphere; the rationale being that the magnetic field is the primary driving force for coronal, and hence heliospheric structure, but also that this is one of the most robustly measured parameters. However, as other relevant parameters mature, such as vector measurements of the magnetic field or density and/or temperature low in the corona, it may be possible to incorporate them into boundary conditions for the model. Preliminary steps in this direction have already been made (e.g., Frazin and Kamalabadi, 2005).

Step a highlights that, upon completion, the coronal model produces a set of outputs that can be directly compared with remote solar observations. These include white-light images, coronal hole boundaries (which can be compared with 10830 He, EUV, and/or soft X-ray observations), and emission images (relevant only if the thermodynamic model was run).

In *step* 2, output from the coronal model is used to generate boundary conditions for one of several heliospheric models. For thermodynamic solutions, the output can be used directly to deduce B_r, v_r, n, and T at $20-30R_\odot$, the inner boundary of the heliospheric model. For polytropic solutions, an *ad hoc* scheme, described by Riley et al. (2001a) is used to derive suitable a speed profile map, and pressure balance and momentum flux conservations are used to deduce n and T.

Our recently-developed heliospheric MHD code, MAS in the Heliosphere (MAS-H), has removed some basic limitations in our ability to model structure in the inner heliosphere. Previously, PSI's heliospheric code was both serial and spectral in the azimuthal dimension. As such, runs were limited to grids in ϕ of n^2, and being serial, memory limitations of workstation computers effectively led to runs of 128 azimuthal points, corresponding to a grid spacing of $\phi = 3^\circ$, or 5 h as measured at Earth. MAS-H can be readily run at average resolutions of $<1^\circ$ in latitude and longitude. CORHEL also supports NOAA's operational inner heliospheric code Enlil, which, in turn, supports cone model CME runs, allowing the user to specify simple configurations for launching ejecta from the inner boundary of the heliospheric code and tracking them as they propagate past 1 AU. Enlil's latitudinal boundaries can be pushed higher, but at increasing computational cost, effectively being limited to $\pm 60^\circ$ in latitude. Thus, for comparisons with Ulysses measurements, for example, (e.g., Riley et al., 2003; Stevens et al., this issue), which require capturing the heliosphere over its entire 4π steradians, it is necessary to use MAS-H.

In *step b* we summarize the main output parameters for the heliospheric model. These include all of the magnetofluid parameters at the location of Earth (or some other location within the heliosphere, nominally out to 5–6 AU) as well as global parameters such as the iso-surface of the heliospheric current sheet (HCS), or large-scale structures such as compression or rarefaction regions.

Physical processes relevant to the outer heliosphere, such as pick-up ions, are not included in our current heliospheric models, rendering them unsuitable beyond perhaps 10 AU. Thus, in an as-yet-to-be-implemented connection, in *step*3 we anticipate how CORHEL could incorporate outer heliospheric models (e.g., Florinski and Pogorelov, 2009), thus being able to compute realistic, event-based solutions all the way from the surface of the Sun out to the edge of the heliosphere.

While it is also possible to envisage CORHEL expanding back through the photosphere and into the convection zone, we believe that, at least currently, photospheric magnetic field measurements are considerably more robust than could be produced from convection/transport models, and, thus, this represents a natural and well-defined boundary. However, that is not to say that the connection could not or should not be made, particularly to study the effects of model-produced photospheric boundary conditions or to study the structure around other magneto-plasma objects, including other stars, for example, where there may be no relevant observations of the surface field.

3. Observations of CIR structure

The several years surrounding CR 2060 (2007–2009) were a period of unusual solar and heliospheric conditions (Riley et al., 2011). The Sun's polar fields were notably weaker than previous near-minima conditions (Svalgaard and Schatten, 2008) and there were significantly more coronal holes producing strong and recurrent high-speed streams.

In Fig. 2 we connect remote solar observations for CR 2060 with *in situ* measurements by the STEREO A and B and ACE spacecraft. Focusing first on the EUV observations, we note several points. First, the northern polar coronal hole is readily visible, while the southern polar coronal hole, if it exists, cannot be seen at all. In fact, during this interval, Earth was situated near its highest point in heliographic latitude [with a B_0 angle (the heliographic latitude of the central point of the solar disk) of 7.1° midway through the rotation]. Thus, the presence of one polar hole and the absence of the other is likely due to an observational selection effect. In fact, analysis of remote solar observations 6 months earlier and later (not shown) reverse the result: the southern polar coronal hole becomes visible at the expense of the northern hole. Second, unlike most previous late declining phases of the solar activity cycle, a number of equatorial and mid-latitude coronal holes were present. Here, we have marked a pair of particularly prominent ones that were relatively persistent from one rotation to the next and generated strong and relatively long high-speed solar wind streams at 1 AU. Third, and related to

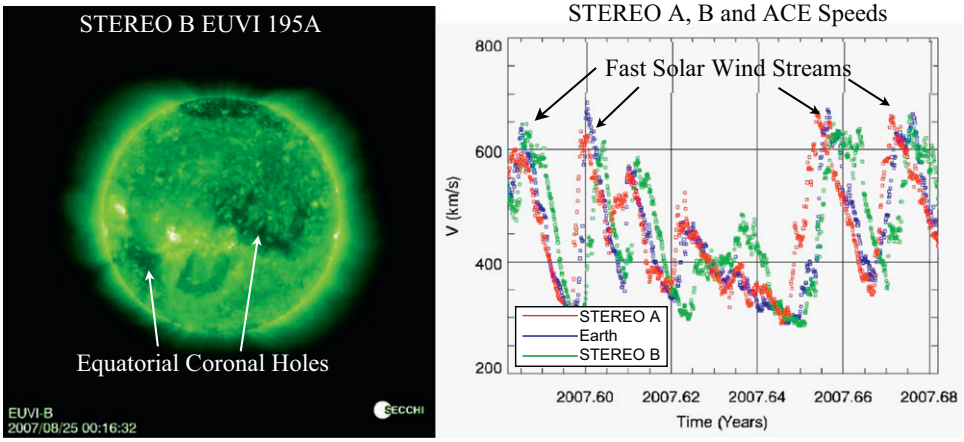

Fig. 2. (Left) EUVI observations from STEREO B at 195 Å on August 25 2007. Two equatorial coronal holes are indicated with the white arrows. (Right) *in situ* measurements of solar wind speed at ~ 1 AU from the two STEREO spacecraft A and B (red and green) and ACE (blue) for CR 2060. The two fast solar wind streams associated with the coronal holes in the image to the left are indicated by the black arrows. (For interpretation of the references to color in this figure legend, the reader is referred to the web version of this article.)

the previous point, several prominent active regions were present during this interval.

STEREO A/B and ACE bulk solar wind speed measurements over the course of one tenth of a year (~ 36.5 days) are shown in the right-hand-side of Fig. 2. Since this interval is $\sim 1/3$ longer than a solar rotation, the two high-speed streams seen at the beginning of the interval are also seen once more (evolved by one rotation) at the end of the interval. Again, we note several points. First, because STEREO A lies ahead of Earth in its orbit, it becomes immersed in a particular high-speed stream first (red trace). ACE then follows (blue), with STEREO B being last (green). The streams are separated in time by an amount proportional to their angular separation. At $\sim 15^\circ$ separation (from ACE to STEREO A or ACE to STEREO B), for example, the streams are delayed from one spacecraft to the next by $15^\circ \times 27.27$ days $/360^\circ \approx 1.2$ days. Second, because of their separation, the large-scale stream structure is roughly the same at all spacecraft: All spacecraft observe the same high-speed streams and inter-speed wind. Third, the largest differences in the profiles occurs midway through the rotation during a period of relatively slow wind when both STEREO A and ACE become immersed in a declining speed profile (2007.62) which lasts for ~ 10 days. While the profiles are virtually identical at STEREO A and ACE, the profile at STEREO B is notably different. In the electronic version of this paper, this figure can also be viewed as a movie highlighting: (1) the evolution of solar wind structure from the launch of the STEREO spacecraft in October 2006 through 2010; and (2) the loss of coherency between the structure measured at the three locations (STEREO A, B, and Earth) as the viewpoints diverge in longitude, and hence time, and, arguably, to a lesser extent, heliographic latitude (Riley et al., 2010b).

4. Model results

In several previous studies, we have described different aspects of the solar corona and heliosphere during this recent declining phase and ensuing minimum (Riley et al., 2010a, 2010b, 2010c, 2011, this issue; Riley, 2010; Riley and Luhmann, 2011). Here, by way of illustration, and to emphasize specific new work, we focus on two aspects: (1) coronal hole boundaries computed from the coronal solution; and (2) the implementation of a new parallel heliospheric code.

One way to assess the quality of the coronal solution is to compare computed coronal hole boundaries with some observed proxy that, in principle, captures the same structure, such as EUV emission images, soft X-ray, or 10,830 He observations.

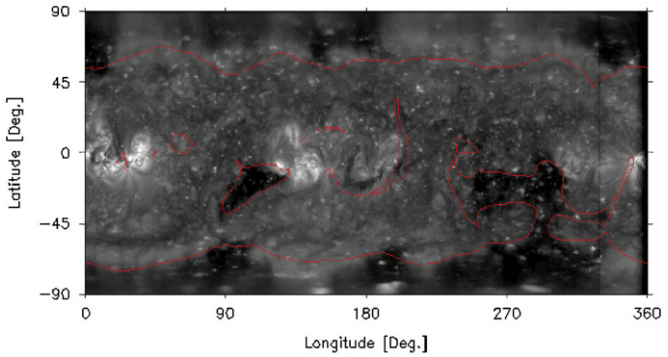

Fig. 3. A comparison of EUVI observations from STEREO A at 195 Å for CR 2051 with the boundaries between open and closed field lines as determined from a polytropic MHD solution (red trace). (For interpretation of the references to color in this figure legend, the reader is referred to the web version of this article.)

In Fig. 3 we compare EUV observations at 195 Å from the SOHO spacecraft with the boundaries of coronal holes from the model. The latter were obtained by tracing out from a longitude-latitude grid at the base of the simulation into the corona. Field lines that extended through the upper boundary ($30R_\odot$) were labeled as "open" while those that closed back down to the solar surface were labeled "closed." In a complementary study, Stevens et al. (this issue) assess the impact of different base densities and temperatures on the quality of the coronal solutions. One measure of this is how well the computed coronal hole boundaries match with EUV emission measurements. In this case, a base temperature of $T_0 = 2.0 \times 10^6$ K was used. This is somewhat higher than our standard values derived from studies based on the minimum marking the end of solar cycle 22 (September, 1996), but produces a qualitatively better match with observations. Focusing on the structure at low and mid latitudes, where there is less likelihood of obscuration from overlying structure, the model captures the two main equatorial coronal holes, and, in particular, the "anvil" shaped structure centered at approximately 285° longitude. There is a mismatch in the location of the northern polar coronal hole, which we believe is likely a combination of poor resolution of this area, coupled with "contamination" from overlying emission. It is worth noting that, at full resolution, EUVI images contain 2048 pixels in sine-latitude, of which approximately 35 pixels lie above 75° latitude at each pole

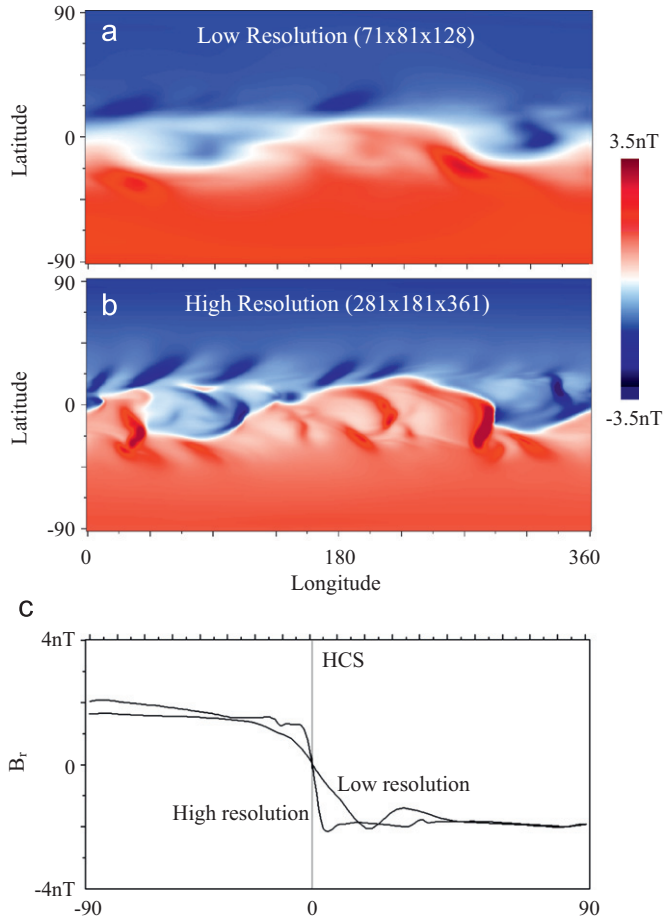

Fig. 4. Comparison of model results at 1 AU using our older serial code (a) and our recently-developed parallel code (b). The serial solution was computed on a grid of $71 \times 81 \times 128$ points whereas the parallel solution was computed with $281 \times 181 \times 361$ points. In (c) Meridional traces from each solution are compared.

when the B_0 angle is zero. When $B_0 \sim 3^\circ$, approximately 22 pixels cover the "obscured" pole and 50 pixels span the "visible" pole. However, the synoptic map shown here retains only 500 pixels in the vertical direction (or 250 from equator to pole), and a mere 5 pixels cover the north pole (above 75°), and 12 pixels cover the south. Thus, we conclude, while the south is poorly resolved, the situation is even worse for the north pole.

A second possibility for the mismatch in the location of the northern polar coronal hole boundary is that the model has overestimated the polar coronal area, presumably because the extrapolated polar fields were too large. As we discuss later, deriving values for the polar fields is a significant challenge for global models, and this explanation for the poor fit cannot be discounted easily, nor can it be readily resolved without direct observations of the Sun's polar regions.

To assess the impact of resolution (as well as some algorithmic changes), in Fig. 4 we compare heliospheric solutions using our older serial code with a recently developed fully parallel code. Although a number of minor improvements were also made between the two codes (such as replacing the spectral solve in azimuth with a finite difference scheme in all three dimensions) the principle improvement has been to allow us to compute solutions at resolutions previously not possible. Here, the numbers of grid points were increased by factors of four, two and a half, and three, in radius, latitude, and azimuth, respectively. Moreover, the lower-resolution solution spanned from $30R_\odot$ to 5 AU, whereas the higher-resolution solution was limited to 1 AU.

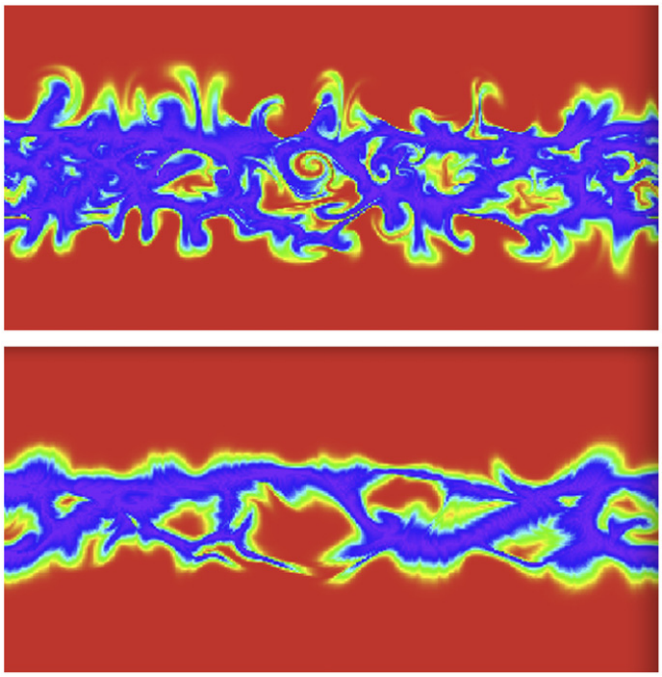

Fig. 5. Comparison of radial speed boundary conditions at $30R_\odot$ for (top) high-resolution simulation and (bottom) low-resolution simulation of CR 2060.

Thus, overall, the number of grid points was effectively increased by a factor of 150. Not surprisingly, the new, more-resolved solutions are producing richer and more complex structure. Although the band of solar wind variability stretches to roughly the same extent in latitude and the grossest features appear in both solutions, beyond that, there are significant differences with obvious impact on the predicted structure of the solar wind at 1 AU in the ecliptic plane.

In Fig. 4(c) we compare traces in latitude at some arbitrary longitude of the radial magnetic field from the two solutions. Although the fields far from the HCS are comparable, nearer to the field reversal, the low-resolution solution spreads out the NS polarity transition, thus leading to smaller predicted field values. Whereas the transition occurs over $\pm 50^\circ$ in the low-resolution solution, it is complete within $\pm 5^\circ$ in the high-resolution. Of course this is still significantly larger than would occur in reality (e.g., Winterhalter et al., 1994), but the change is clearly in the right direction.

The differences between the low- and high-resolution solutions at 1 AU is likely due to two coupled effects. First, higher spatial resolution is maintained in deriving the boundary conditions for the higher-resolution heliospheric solution. And second, the finer-scale structure contained in those boundary conditions is retained as the structure evolves from $30R_\odot$ to 1 AU. In Fig. 5 we compare the main boundary condition driver for the heliospheric solution; the bulk (radial) solar wind flow. Since CIR structure is driven primarily by the velocity profile (Riley, 2010), even a cursory comparison of the two maps suggests that the solutions (at least at low and mid-latitudes) will be different. However, until we compare with actual observations, we cannot be sure whether the added structure adds or subtracts value from the solution.

5. Comparison with observations

We now turn our attention to more direct comparisons of the model results with observations. For the coronal solution, we

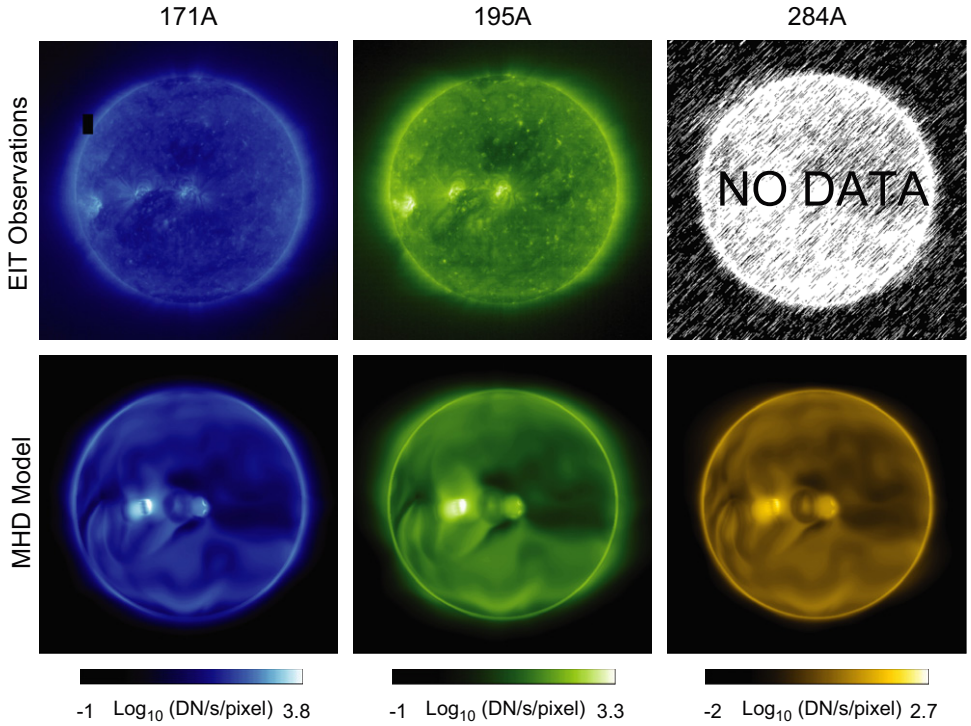

Fig. 6. Comparison of SOHO/EIT observations at 171, 195, and 284 Å with simulated emission images from a global MHD solution (driven by data from MDI) of CR 2068.

compare simulated EUV emission with observations for CR 2068. This requires use of the thermodynamic model since the polytropic solutions cannot reproduce sufficient contrast in density and temperature to yield simulated emission of any value. The quality of the results is also quite sensitive to the thermodynamic parameters chosen (Lionello et al., 2009) and such comparisons are thus a good test of the heating model. For the heliospheric solution, we compare simulated *in situ* measurements of bulk solar wind speed, v, and the magnitude and polarity of the radial component of the interplanetary magnetic field, B_r, both of which have value from a space weather perspective. Ideally, we would also compare B_z, which, together with v_r yields the dawn-dusk electric field imposed across the magnetosphere—the primary driver for geomagnetic activity, and hence the main input parameter for event-based global magnetospheric models (Wiltberger et al., this issue). However, currently, global heliospheric models are not able to generate substantial B_z fields in CIRs, presumably because turbulence and/or wave effects, which provide a seed field that can be enhanced by compression regions and fast CMEs, are not incorporated. Only a modest B_z component is produced from the Russell–McPherron effect (Russell and McPherron, 1973).

Simulated emission images for CR 2068 (i.e., Whole Heliosphere Interval) are compared with SOHO/EIT observations at the same time in Fig. 6. Unfortunately, no data were available from EIT at 284 Å. It is important to note that the comparison is quantitative, and not qualitative, that is, actual counts/second/pixel are compared. Overall, we believe that the model has captured the basic structure of the solar corona as manifested in emission measurements. The general brightness of the disk, limb, and the relative intensity of the active regions compare favorably, as do the basic locations of the coronal holes. One 'glaring' disagreement is the third, east-most active region. While that data clearly show a triplet of active regions, the model has only produced two. Active region heating in the model is sensitive to the local magnetic field strength. Thus, while it is possible that a threshold value was not reached which would have 'lit up' the active region, it is more likely a problem due to the fact that the synoptic map used to generate the solution relied on central meridian data that was more than 21 days old. In reality, the active region seen in the observations probably appeared or evolved while on the far side of the Sun.

Considering next the *in situ* measurements, in Fig. 7 we compare model solutions for CR 2060 using a synoptic photospheric magnetic field map derived from Wilcox Solar Observatory (WSO) measurements. The model matches the stream structure reasonably well. In particular, the initial long-duration of slow wind, followed by a strong and steep high-speed stream on 08/26/2007. The second stream is overestimated by the model, as is the third, to an even greater extent. The polarity of the radial magnetic field measured during this interval consisted of a simple two-sector pattern, initially inward, and switching to outward around 08/30/2007. The smaller-scale reversals not mimicked into model results probably represent waves and/or turbulence, which, as we have noted, are not included in the MHD model. On the left, the global structure of the solar wind velocity from the model is shown at $30R_{\odot}$. This frame corresponds to the blue vertical band in the time series. A movie showing how the global structure of solar wind speed varies as a function of time is included in the electronic version of the paper.

While the previous comparison revealed a few discrepancies between the model results and the observations, as a whole, the match was relatively good, and, particularly in terms of the timing of the fronts of the high-speed streams, which is a feature of significant value from a space weather prediction standpoint. However, the comparison is not always as fair. Even for the same interval, using an input synoptic magnetic field derived from data measured by a different observatory can have a profound effect on the solution. In Fig. 8 we compare the same *in situ* measurements but with model results computed using data from the MDI instrument onboard the SOHO spacecraft. Clearly the model solution fails to reproduce much of the observed stream structure. Although it predicts a stream midway through the rotation, if it is associated with the observed first stream, it lags significantly.

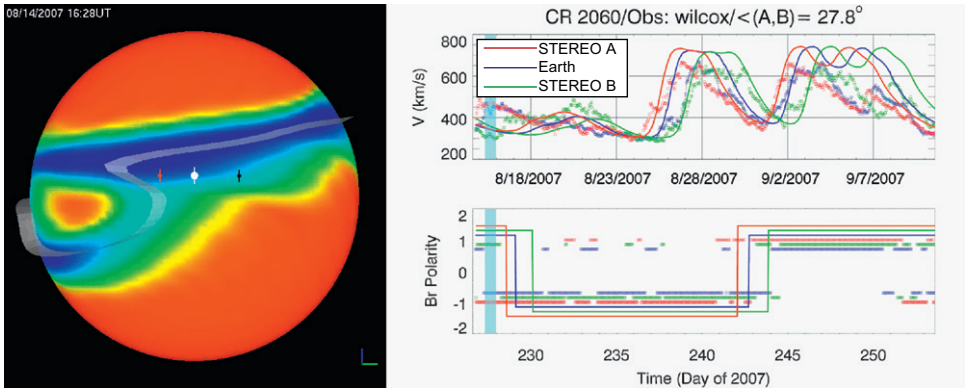

Fig. 7. Times series comparison of solar wind speed and IMF polarity at 1 AU for CR 2060. The model results (solid lines) were obtained by flying the STEREO A, B, and ACE spacecraft through the simulation region. The *in situ* measurements have been smoothed using box-car averages of 12 h. On the left, the global model velocity profile at $30R_{\odot}$ is shown, together with the location of the heliospheric current sheet (grey iso-surface), and the mapped back location of the three spacecraft. In the electronic version of this paper, a movie based on this Figure illustrates how the global solar wind speed pattern changes underneath the spacecraft.

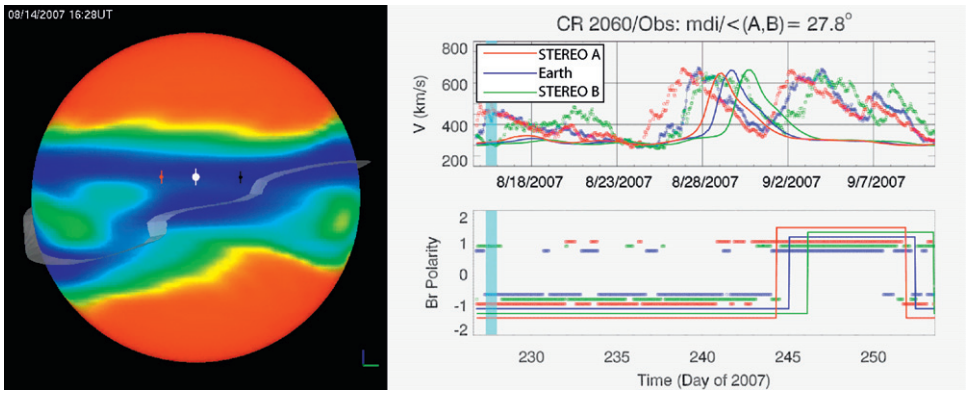

Fig. 8. As Fig. 7 but for a model solution driven by data from SOHO's MDI instrument.

Moreover, none of the subsequent high-speed stream structure appears in the model solution. And, although the model is consistent with a two-sector pattern, the phasing of the sector crossings does not match the observations nearly so well.

We can understand the source of the poor match with the MDI model results from the movie from which Fig. 7 and 8 were extracted. In both solutions, the first stream corresponds to wind from an equatorial coronal hole. However, in the Wilcox solution this stream is faster and broader. The slow-flow band is relatively flat and structureless in the MDI solution, while in the Wilcox solution it is significantly more warped and punctuated by more variable-speed wind. This provides a source of fast wind from the southern polar coronal regions for the last third of the rotation, consistent with the observations. Additionally, the HCS, which traces through the slow-flow band in both solutions extends to higher heliographic latitudes in the Wilcox solution, thus allowing the simulated spacecraft to remain in an outward polarity for a longer period of time.

Tracing the source of these differences to the velocity boundary of the heliospheric solution, however, provides only a partial answer to why the solutions differ so much. Since the only fundamental difference between the two model results lies in the input magnetogram, we must turn to them for a more complete answer. In Fig. 9 we compare the processed synoptic magnetograms for the MDI and Wilcox solutions (top-left and bottom-right). We have also included maps from NSO's SOLIS and GONG facilities for comparison. We also computed solutions using data from SOLIS and GONG (results not shown). SOLIS results were very similar to the results obtained using MDI, that is, relatively poor. Results obtained from GONG were better. In particular, the stream structure during the final third of the rotation was reproduced very well. It is worth reiterating that these are processed synoptic maps. We have applied a pole-fitting algorithm to them to fill in missing, or poorly resolved data and smoothed the entire map to remove high-spatial frequency structure that might cause numerical issues. Focusing first on a comparison of the magnetograms from MDI and Wilcox, beyond the initial similarities in the general features of the largest-scale active regions, we note several differences. First, Wilcox, with its limited resolution captures only the largest-scale structure. Second, whereas the MDI map contains strong and relatively comparable strength polar fields, the polar fields in the Wilcox map are not balanced, with the southern polar field being significantly weaker. More generally, considering the GONG and SOLIS maps, we note that the poles are relatively weak at GONG, but stronger at SOLIS. Moreover, the low- and mid-latitude field strengths are stronger at SOLIS. Generally, both GONG and Wilcox display weaker polar fields everywhere; however, and more importantly, the ratio of the strength of the polar to equatorial fields is lower for GONG/Wilcox than for MDI/SOLIS. With proportionally smaller polar fields, as in GONG/Wilcox, near-equatorial structure can open up and exert more control on the heliospheric solution. Consequently, this has the effect of: (1) opening up equatorial coronal holes further producing stronger high-speed streams; (2) allowing the band of solar wind variability (i.e., the slow, but variable wind) to rise and fall more in latitude; and (3) in turn, allowing the HCS to reach higher heliographic latitudes.

Finally, to assess whether the high-resolution solutions are leading to more accurate solutions near Earth, in Fig. 10 we compare solar wind speed, the radial component of the

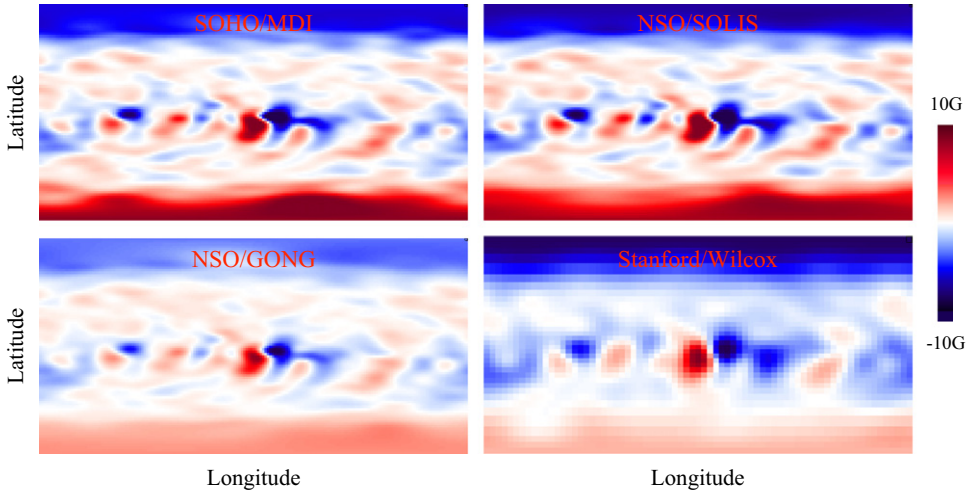

Fig. 9. Comparison of four processed synoptic maps: top-left: SOHO/MDI; top-right: NSO/SOLIS; bottom-left: NSO/GONG; and bottom-right: Stanford/Wilcox.

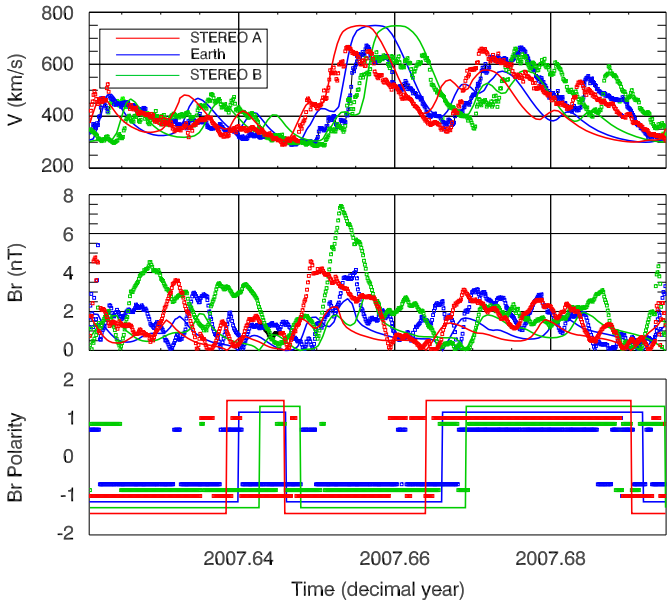

Fig. 10. Times series comparison of solar wind speed, absolute magnitude of the radial component of the magnetic field, and magnetic polarity at 1 AU for CR 2060 using high-resolution heliospheric simulation results. The model results (solid lines) were obtained by flying the STEREO A, B, and ACE spacecraft through the simulation region. The *in situ* measurements (squares) have been smoothed using box-car averages of 12 h.

interplanetary magnetic field (IMF), and the polarity of the magnetic field with observations from STEREO A, B, and ACE. For this solution magnetograms from MDI were used. Comparing with Fig. 8, we see that the added resolution appears to have improved the solution in several key areas. First, the timing of the primary high-speed stream is better phased now in the simulations (particularly at STEREO A). Second, the model solution now produces a double rise at the leading edge of this high-speed stream. Third, speeds of the remaining streams are now more modest in the model solutions, in better agreement with the observations. Fourth, the model solution now includes variability on the scale of several days, and, while the phasing of these peaks and troughs does not obviously match the observations, it is promising that the model solution is at least producing power at these frequencies. In the middle panel, we have also included a comparison of B_r. One of the problems with the heliospheric solutions is that they currently produce field strengths that are a factor of 3 or more lower than measurements at 1 AU. We had anticipated that the higher-resolution solutions would better resolve HCS crossings and limit any numerical diffusion of fields. However, as can be seen, while there is a modest increase in the average field strength, resolution alone cannot explain the mismatch between observations and model solutions.

6. Summary and discussion

In this study, we have applied CORHEL, a suite of MHD models of the solar corona and inner heliosphere, to study CR 2060, and, more generally, the late declining phase and solar minimum of solar cycle 23. Our model results were able to reproduce the essential features of the observed stream structure at 1 AU, as well as the basic structure of the solar corona, as inferred from both comparisons of EUV and white-light observations. As such, they provided a global backdrop with which to interpret and connect remote solar observations and *in situ* measurements. An equally important aspect of our study, however, was to assess some of the current limitations with our modeling procedure. We identified five main areas: (1) boundary conditions derived from synoptic magnetograms from different observatories can give significantly different results; (2) although a particular observatory may perform better for a given rotation, we have not identified one observatory that systematically performs better; (3) the solutions (both coronal and heliospheric) are sensitive to how polar fields are reconstructed; (4) our previous heliospheric solutions, while able to reproduce the grossest-scale features, including the location of the HCS, were limited in their ability to capture meso-scale structure, particularly surrounding the HCS; and (5) heliospheric models, or their inputs, underestimate the radial component (and strength) of the interplanetary magnetic field by a significant factor.

Although our model results have revealed an underlying sensitivity to the magnetogram used to drive the solution, we have not yet identified what aspects of the raw magnetograms or our processing procedure are responsible for producing either better or worse matches with observations. We believe that the polar fields, which are poorly, if at all observed are a crucial component. The noise in raw magnetograms increases significantly with latitude as each latitude bin, as viewed from Earth, becomes increasingly smaller. Moreover, if our assumption that the observed line-of-sight field is in fact radial (which is, in itself a

questionable assumption Harvey et al., 2007), this further compounds the problem: errors in the measurements are multiplied as an increasingly smaller component is converted into a radial vector. Our current technique for addressing these issues is to extrapolate mid-latitude fields to the polar regions; however, this sometimes introduces its own set of errors. It is unlikely, for example, that the polar fields during CR 2060 were as asymmetric as inferred from the map derived from Wilcox observations (lower-left panel of Fig. 9). In spite of this, that map produced, arguably the best match with *in situ* measurements, presenting us with a quandary.

For the purposes of interpreting the global structure of the heliosphere during specific time periods, it may be reasonable to run an ensemble of cases using synoptic maps from different observatories with a range of reasonably defensible processing steps, and choose the solution that best matches most of the observations or some specific aspect under study. This solution can then likely be analyzed with confidence. However, this is clearly not an ideal mode of operation, and, if there is no consistency in the choice of input magnetogram or how it is processed, global MHD models (and PFSS models for that matter) will have limited predictive capability.

Although related to the above point, a distinct issue regarding the preparation of the input magnetograms is how the polar fields are reconstructed. Importantly, our current automated procedure for processing the raw synoptic magnetogram maps frequently produces questionable polar field estimates. While we are currently assessing different approaches for resolving this, a few points are in order. First, there is no shortage of possible techniques to choose from. Liu et al. (2007) compared seven methods for computing polar fields based on various extrapolation techniques. They concluded that a time-dependent interpolation technique relying on the observed polar fields was the best approach. More recently, Sun et al. (2011) have developed a technique using 2-D spatial and temporal interpolation, coupled with a simple flux transport model to compute the unseen values. In contrast, the group at NSO employ two distinct techniques for SOLIS and GONG data, a historical result of the processing routines being developed, at least in part, independently, rather than any systematic choice of the best approach. Second, any successful technique should address the $\pm 7.25^{\circ}$ tilting of the poles such that every 6 months one pole is obscured while the other is (at least partially) observed. Arge and Pizzo (2000) implemented a scheme in the WSA model that uses data from earlier periods when a particular pole was observed to help constrain the polar values when they cannot be measured from Earth. Third, a successful extrapolation technique might weight data based on a noise estimate of the surrounding pixels, giving greater weight effectively to lower latitude pixels for which noise estimates will be lower. Fourth, rather than extrapolating in latitude at a specific time, a more sophisticated approach might extrapolate forward in time as well, incorporating the "run to the poles" streaks that can be seen in the so-called butterfly diagrams of the longitudinally-averaged field on the time scale of a solar cycle or more. Fifth, and finally, flux transport models (e.g., Schrijver and Liu, 2008; Arge et al., 2010) may ultimately offer the best pole-to-pole boundary conditions. Not only can they in principle self-consistently fill in the polar regions based on the migration of lower-latitude magnetic structure, but they can also provide truly synoptic (that is, "at the same time") maps, rather than the asynchronic ("at different times") maps that must necessarily be produced from observations limited by our Earth-centric view of the Sun. Moreover, maps developed by flux transport techniques are intrinsically functions of time, allowing the specification of self-consistent time-dependent boundary conditions for the MHD models.

Although we have not yet made a detailed study, the appearance of the finer-scale structure in the high-resolution heliospheric simulation results is intriguing. Should it account for some or all of the structure seen in the band of solar wind variability, this would allow us to resolve a long-standing question on the origin of the variability of the slow wind: does it originate from temporal or spatial variations at the source, or some combination thereof? Merkin et al. (2011) applied a global MHD model of the inner heliosphere to study the disruption of a heliospheric current sheet fold. They found that at least some finer-scale structure could be self-generated in the solar wind. Preliminary analysis of our results, in contrast suggests that, at least some of the observed structure is reproduced by quasi-steady structure at the inner boundary. However, with only a single-solution to study, any inferences would be premature. We are currently planning a sequence of simulations, which we hope will provide us with meaningful insight into this question.

One of the motivations for developing the new parallel heliospheric code was to assess whether the resolution of the simulations was contributing to the anomalously low field strengths (by a factor of three or more) predicted by the model at 1 AU. To the best of our knowledge, these low values have plagued most heliospheric models, and, until now, no systematic analysis of its origin had been performed. We identified several possible causes for the low computed field strengths. First, a potential source of error lies in the inability of the low-resolution solutions to capture the sharp transition at sector boundaries. Integrating the magnitude of B_r for the two profiles in panel (c) of Fig. 4, for example, would show a net decrease of 5–10% in the average unsigned flux of the low-resolution case. Thus, while it might contribute to lower predicted values, its effect is not sufficient to account for $\times 3$ deficit. Additionally, since the mismatch still occurs over the poles of the Sun during near solar minimum conditions, well away from the HCS, its contribution can be, at most, a minor effect.

A second potential origin for the low model field strengths is that the input magnetograms to the coronal model might be systematically low. We have performed both inter-calibration studies using magnetogram measurements from different observatories, as well as computing global coronal and heliospheric solutions using data from different observatories (Riley et al., submitted for publication), but found only modest effects. A third possibility is that the free parameters in the models might not be allowing enough coronal field to open up into the solar wind, resulting in a lower open flux. In a complementary study, we have investigated the effects of changing the density and temperature at the base of the calculation on the amount of flux opening into the heliosphere (Stevens et al., this issue). We found that, indeed, a modest 10% increase in the base temperature appears to rise the open flux sufficiently to potentially resolve this issue without otherwise reducing the match between other parameters, such as the boundary of coronal holes. Finally, it is worth noting that while we have not yet firmly identified the origin of the low interplanetary field strengths, it is not obviously related to any issues within the heliospheric models themselves, since the problem already exists at their inner radial boundary.

As a final comment, although we have devoted a considerable portion of this study to addressing the deficiencies in current global modeling techniques, we should not overlook the basic successes in being able to reproduce coronal and heliospheric structure during quiescent conditions. The recent delivery of an operational version of the WSA/Enlil coupled models (both of which are included in CORHEL) to NOAA's weather service (Farrell, 2011), a "first" for space weather models, is a testament to the fact that our ability to predict solar wind conditions in the vicinity of Earth is improving. What we have shown here is that

while progress is being made, we still must address a number of important hurdles before we can claim to have succeeded.

Acknowledgments

The authors gratefully acknowledge the support of NSF under the Center for Integrated Space Weather Modeling (CISM) program, the LWS Strategic Capabilities Program (NASA, NSF, and AFOSR), NASA's Heliophysics Theory Program (HTP), and the STEREO IMPACT team. Additionally, PR acknowledges support from NASA's Causes and Consequences of the Minimum of Solar Cycle 24 program. Finally, PR would also like to thank Dr. J. Américo Gonzalez Esparza and the Universidad Nacional Autónoma de México (UNAM) for providing support and facilities while this study was being completed.

Appendix A. Supplementary material

Supplementary data associated with this article can be found in the online version of 10.1016/j.jastp.2011.12.013.

References

Arge, C.N., Henney, C.J., Koller, J., Compeau, C.R., Young, S., MacKenzie, D., Fay, A., Harvey, J.W., 2010. Air force data assimilative photospheric flux transport (ADAPT) model. Twelfth International Solar Wind Conference 1216 (March), 343–346.

Arge, C.N., Pizzo, V.J., 2000. Improvement in the prediction of solar wind conditions using near-real time solar magnetic field updates. Journal of Geophysical Research 105, 10465.

Farrell, P., 2011. New Space Weather Forecasting Model Going Operational with National Weather Service. 〈www.bu.edu/cas/news/press-releases/cism/〉.

Florinski, V., Pogorelov, N.V., 2009. Four-dimensional transport of galactic cosmic rays in the outer heliosphere and heliosheath. Astrophysical Journal 701 (August), 642–651.

Frazin, R.A., Kamalabadi, F., 2005. On the use of total brightness measurements for tomography of the solar corona. Astrophysical Journal 628 (August), 1061–1069.

Gibson, S.E., de Toma, G., Emery, B., Riley, P., Zhao, L., Elsworth, Y. Leamon, R.J., Lei, McIntosh, S., Mewaldt, R.A., Thompson, B.J., Webb, D. 2011. The whole heliosphere interval in the context of a long and structured solar minimum: an overview from sun to earth. Solar Physic, 422. doi:10.1007/s11207-011-9921-4. 〈http://adsabs.harvard.edu/abs/2011SoPh..tmp..422G〉, (Provided by the SAO/NASA Astrophysics Data System).

Gibson, S.E., Kozyra, J.U., de Toma, G., Emery, B.A., Onsager, T., Thompson, B.J., 2009. If the Sun is so quiet, why is the Earth ringing? A comparison of two solar minimum intervals. Journal of Geophysical Research 114 (September), 9105.

Gosling, J.T., Bame, S.J., McComas, D.J., Phillips, J.L., 1990. Coronal mass ejections and large geomagnetic storms. Geophysical Research Letters 17, 901.

Harvey, J.W., Branston, D., Henney, C.J., Keller, C.U., 2007. SOLIS and GONG Teams, 2007. Seething horizontal magnetic fields in the quiet solar photosphere. Astrophysical Journal Letters 659 (April), L177–L180.

Lario, D., Roelof, E.C., 2007. Energetic particles during the first and third Ulysses southern high-latitude excursions: probing global corotating interaction region structure beyond 5 AU. Journal of Geophysical Research 112 (September), 9107.

Lindsay, G.M., Russell, C.T., Luhmann, J.G., 1995. Coronal mass ejection and stream interaction region characteristics and their potential geomagnetic effectiveness. Journal of Geophysical Research 100 (Sep.), 16999–17014.

Lionello, R., Linker, J.A., Mikić, Z., 2009. Multispectral emission of the sun during the first whole sun month: magnetohydrodynamic simulations. Astrophysical Journal 690 (January), 902–912.

Liu, Y., Hoeksema, J.T., Zhao, X., Larson, R.M., 2007. MDI Synoptic Charts of Magnetic Field: Interpolation of Polar Fields. American Astronomical Society Meeting Abstracts #210. Bulletin of the American Astronomical Society, vol. 38; 2007, pp. 129.

Merkin, V.G., Lyon, J.G., McGregor, S.L., Pahud, D.M., 2011. Disruption of a heliospheric current sheet fold. Geophysical Research Letters 381 (July), 14107.

Riley, P., 2010. The three-dimensional structure of the inner heliosphere. in: Maksimovic, M., Issautier, K., Meyer-Vernet, N., Moncuquet, M., Pantellini, F. (Eds.), Twelfth International Solar Wind Conference, American Institute of Physics Conference Proceedings, vol. 1216; 2010, pp. 323.

Riley, P., Linker, J.A., Gonzalez-Esparza, J.A., Jian, L., Russell, C., Luhmann, J. Interpreting some properties of CIRs and their associated shocks during the recent solar minimum using global MHD simulations. Journal of Atmospheric and Terrestrial Physics, this issue.

Riley, P., Linker, J.A., Mikić, Z., 2001a. An empirically-driven global mhd model of the corona and inner heliosphere. Geophysical Research Letters 106, 15889.

Riley, P., Linker, J.A., Mikić, Z., Lionello, R., 2001b. Mhd modeling of the solar corona and inner heliosphere: Comparison with observations. in: Song, P., Singer, H.J., Siscoe, G.L. (Eds.), Space Weather, Geophysical Monograph Series, vol. 125. AGU, Washington, DC, pp. 159.

Riley, P., Linker, J.A., Mikic, Z., 2010a. Global MHD modeling of the solar corona and inner heliosphere for the whole heliosphere interval. Highlights of Astronomy 15, 491–493. doi:10.1017/S1743921310010367. 〈http://adsabs.harvard.edu/abs/2010HiA....15..491R〉. (Provided by the SAO/NASA Astrophysics Data System).

Riley, P., Lionello, R., Linker, J.A., Mikic, Z., Luhmann, J., Wijaya, J., 2011. Global MHD modeling of the solar corona and inner heliosphere for the whole heliosphere interval. Solar Physics, 145.

Riley, P., Luhmann, J.G., 2011. Interplanetary signatures of unipolar streamers and the origin of the slow solar wind. Solar Physics, 417 doi:10.1007/s11207-011-9909-0. 〈http://adsabs.harvard.edu/abs/2011SoPh..tmp..417R〉. (adsnote = Provided by the SAO/NASA Astrophysics Data System).

Riley, P., Luhmann, J., Opitz, A., Linker, J.A., Mikic, Z., 2010b. Interpretation of the cross-correlation function of ACE and STEREO solar wind velocities using a global MHD Model. Journal of Geophysical Research (Space Physics) 115 (November), 11104.

Riley, P., Mikić, Z., Linker, J.A., 2003. Dynamical evolution of the inner heliosphere approaching solar activity maximum: interpreting ulysses observations using a global mhd model. Annals of Geophysics 21, 1347.

Riley, P., Mikic, Z., Linker, J.A., Harvey, J., Henney, C.J., Hoeksema, T., Liu, Y., Ulrich, R., Bertello, L. A multi-observatory inter-calibration of line-of-sight diachronic solar magnetograms and implications for the open flux of the heliosphere. Astrophysical Journal. Submitted for publication.

Riley, P., Mikic, Z., Linker, J.A., Schwadron, N.A., McComas, D.J., 2010c. On the relationship between coronal heating, magnetic flux, and the density of the solar wind. Journal of Geophysical Research 115, 6104. doi:10.1029/2009JA015131.

Russell, C.T., McPherron, R.L., 1973. Semiannual variation of geomagnetic activity. Journal of Geophysical Research 78, 92–108.

Schrijver, C.J., Liu, Y., 2008. The global solar magnetic field through a full sunspot cycle: observations and model results. Solar Physics 252 (October), 19–31.

Stevens, M., Linker, J.A., P., R. A study of the sensitivity of global MHD model solutions of the solar corona to boundary conditions. Journal of Atmospheric and Terrestrial Physics, this issue.

Sun, X., Liu, Y., Hoeksema, J.T., Hayashi, K., Zhao, X., 2011. A new method for polar field interpolation. Solar Physics 270 (May), 9–22.

Svalgaard, L., Schatten, K.H., 2008. Predicting solar cycle 24. AGU Fall Meeting Abstracts, A1593.

Tsurutani, B.T., Gonzalez, W.D., Gonzalez, A.L.C., Guarnieri, F.L., Gopalswamy, N., Grande, M., Kamide, Y., Kasahara, Y., Lu, G., Mann, I., McPherron, R., Soraas, F., Vasyliunas, V., 2006. Corotating solar wind streams and recurrent geomagnetic activity: a review. Journal of Geophysical Research 111 (June), 7.

Wiltberger, M., Huang, C.L., Qain, L., Wang, W., Burns, A.G., Solomon, S.C. CMIT study of CR2060 and 2068 comparing L1 and MAS solar wind drivers. Journal of Atmospheric and Terrestrial Physics, doi:10.1016/j.jastp.2012.01.005, this issue.

Winterhalter, D., Smith, E.J., Burton, M.E., Murphy, N., McComas, D.J., 1994. The heliospheric plasma sheet. Journal of Geophysical Research 99 (April), 6667.